

THE ROLE OF DIFFUSIVE SHOCK ACCELERATION ON NON-EQUILIBRIUM IONIZATION IN
SUPERNOVA REMNANTSDANIEL J. PATNAUDE¹, DONALD C. ELLISON², & PATRICK SLANE¹*Draft version February 14, 2009*

ABSTRACT

We present results of semi-analytic calculations which show clear evidence for changes in the non-equilibrium ionization behind a supernova remnant forward shock undergoing efficient diffusive shock acceleration (DSA). The efficient acceleration of particles (i.e., cosmic rays) lowers the shock temperature and raises the density of the shocked gas, thus altering the ionization state of the plasma in comparison to the test particle approximation where cosmic rays gain an insignificant fraction of the shock energy. The differences between the test particle and efficient acceleration cases are substantial and occur for both slow and fast temperature equilibration rates: in cases of higher acceleration efficiency, particular ion states are more populated at lower electron temperatures. We also present results which show that, in the efficient shock acceleration case, higher ionization fractions are reached noticeably closer to the shock front than in the test-particle case, clearly indicating that DSA may enhance thermal X-ray production. We attribute this to the higher postshock densities which lead to faster electron temperature equilibration and higher ionization rates. These spatial differences should be resolvable with current and future X-ray missions, and can be used as diagnostics in estimating the acceleration efficiency in cosmic-ray modified shocks.

Subject headings: cosmic rays – thermal emission: ISM – shock waves – supernova remnants – X-rays: ISM

1. INTRODUCTION

In young supernova remnant (SNR) shocks, the acceleration of cosmic rays leads to a softening of the equation of state in the shocked plasma. This comes about because the diffusive shock acceleration (DSA) process turns some non-relativistic particles into relativistic ones and because some of the highest energy relativistic particles escape from the shock. Both of these effects lead to lower post-shock plasma temperatures as well as higher post-shock densities (e.g., Jones & Ellison 1991; Berezhko & Ellison 1999). The ionization state of shocked gas at a particular time is dependent upon both the gas density and the electron temperature. In light of this, DSA ought to leave its imprint on the ionization structure of the shocked gas. Toward this end, we present what we believe to be the first self-consistent model for SNR evolution which includes the hydrodynamics, the effects of efficient shock acceleration, and a full treatment of the non-equilibrium ionization balance at the forward shock.

A number of young SNRs show both nonthermal and thermal emission in the region behind the forward shock, including SN 1006 (Vink et al. 2003; Bamba et al. 2008), Tycho (Hwang et al. 2002; Cassam-Chenaï et al. 2007), and Kepler (Reynolds et al. 2007). The thermal emission arises when the forward shock sweeps up the circumstellar medium (CSM) and heats it to X-ray emitting temperatures. As pointed out in Ellison et al. (2007) (hereafter DCE07), the thermal emission is often considerably fainter than the nonthermal emission, but there are certainly examples where the thermal emission is as bright

or brighter than any nonthermal emission (Vink et al. 2006). In SNR RX J1713.7-3946, the lack of thermal X-ray emission is an important constraint on the ambient density and significantly impacts models for TeV emission (e.g., Slane et al. 1999; Ellison, Slane & Gaensler 2001; Aharonian et al. 2007; Katz & Waxman 2008).

If the diffusive shock acceleration process in young SNRs is as efficient as generally believed, with $\gtrsim 50\%$ of the shock ram kinetic energy going into relativistic particles, nonlinear DSA will influence the SNR hydrodynamics and be important for non-equilibrium ionization (NEI) calculations (e.g., Decourchelle, Ellison & Ballet 2000; Ellison & Cassam-Chenaï 2005). DCE07 took the first steps in self-consistently coupling nonlinear DSA with NEI by tracking the electron temperature (T_e) and ionization age (defined as $n_e t$, where n_e is the electron density and t is the time since the material was shocked) as a function of time in hydrodynamic simulations of SNRs where the forward shock was efficiently producing cosmic rays (CRs) and, as a result, was substantially modified from test-particle results. They found that, while both T_e and $n_e t$ did differ between the test-particle and CR-modified cases, in the cases where DSA is highly efficient, the synchrotron emission in the X-ray range is considerably stronger than the thermal X-ray spectrum, and any differences in the thermal X-rays as a result of CR-modification are likely to be missed. In this paper, we extend the work of DCE07 by explicitly tracking the non-equilibrium ionization state in a CR-modified shock. The lower shock temperature and higher density that result from efficient DSA combine to shorten both the temperature equilibration and ionization equilibrium time-scale, and we show that this can have a dramatic effect on the ionization structure between the forward shock (FS) and the contact discontinuity (CD). Although we don't calculate the thermal X-ray emission

¹ Smithsonian Astrophysical Observatory, Cambridge, MA 02138

² Physics Department, NC State University, Box 8202, Raleigh, NC 27695; don_ellison@ncsu.edu

here, the cases we study show that efficient DSA can increase the ionization fraction of important elements and possibly enhance thermal X-ray emission.

In § 2, we outline the changes to our model first presented in DCE07 and discuss several caveats to our approach. In § 3, we present our examples and discuss the quantitative and qualitative effects of efficient DSA on the ionization state and SNR structure. We also show how these effects might manifest themselves in current and future X-ray observations. In § 4, we summarize our results and outline our future enhancements to this model.

2. CR-HYDRO + NEI MODEL

Our spherically symmetric model uses the semi-analytic DSA calculation developed by Amato & Blasi (2005) and Blasi et al. (2005) and is similar to that used in DCE07, except that we now calculate the non-equilibrium ionization explicitly at every time step using plasma parameters that are continually updated as the SNR evolves. In DCE07, the NEI was calculated at the end of the simulation using average plasma parameters. We refer the reader to DCE07 for all details of the CR-hydro simulation apart for those discussed below detailing our dynamic NEI generalization.

The DSA model used here differs from that described in Ellison et al. (2007), Ellison & Cassam-Chenaï (2005), and previous papers, in two important ways. First, we replace the “effective gamma,” γ_{eff} , approximation with a more realistic model of the effect escaping particles have on the shock dynamics. We now explicitly remove from the shocked plasma the energy that escaping particles carry away from the forward shock. The ratio of specific heats of the shocked gas used in the simulations, γ_{sk} , is determined directly from the particle distribution function including the correct mix of relativistic and non-relativistic particles. While the old effective gamma had the range $1 < \gamma_{\text{eff}} \leq 5/3$, the ratio of specific heats γ_{sk} is constrained to lie between $4/3$ and $5/3$. These changes in the way escaping particles are treated, and γ_{eff} is calculated, become important for later stages of the SNR evolution, but do not produce significant changes in times as short as 1000 yr. The results reported in Ellison et al. (2007) are not modified significantly by these changes.

The second difference is that instead of specifying a fixed injection parameter, χ_{inj} (this is ξ in equation (25) in Blasi et al. 2005), which then determines the acceleration efficiency, we now specify a fixed diffusive shock acceleration efficiency, ϵ_{DSA} , and then determine χ_{inj} accordingly. This change makes the parameterization of the acceleration efficiency more transparent but does not change the basic approximation that is made.

The semi-analytic DSA model we use does not calculate the acceleration efficiency self-consistently based upon the Mach number, the available acceleration time, and other relevant shock parameters; rather we parametrize the efficiency by χ_{inj} , and the model then determines the shock structure self-consistently. Furthermore, the DSA model assumes that the thermal particles have a Maxwell-Boltzmann distribution with a superthermal tail. The actual shape of the quasi-thermal distribution, and the shape at the point where the superthermal tail joins it, are approximated since the semi-analytic calculation only self-consistently describes par-

ticles with speeds greater than the shock speed, i.e., $v_p \gg v_{\text{sk}}$. The differences at low energies between what is assumed in the DSA model and the actual quasi-thermal distribution are expected to be small, but these differences may become more important if the contribution to ionization from superthermal particles is considered. Despite the approximations of the semi-analytic calculation at quasi-thermal energies, it is the state-of-the-art since the actual quasi-thermal distribution can only be determined with plasma simulations and these are not yet available for SNR parameters.

The ionization structure of shock heated gas at a particular distance behind the shock in a SNR is determined by the electron density n_e , the electron temperature T_e , and the ionization and recombination rates for each ion of interest. The structure is determined by solving the collisional ionization equations in a Lagrangian gas element behind the shock:

$$\frac{1}{n_e} \frac{Df(X^i)}{Dt} = C(X^{i-1}, T_e) f(X^{i-1}) + \alpha(X^i, T_e) f(X^{i+1}) - [C(X^i, T_e) + \alpha(X^{i-1}, T_e)] f(X^i). \quad (1)$$

Here, $f(X^i)$ is the fraction of element X in ion stage X^i and $C(X^i, T_e)$ and $\alpha(X^i, T_e)$ are the ionization and recombination rates out of and into ion X^i , respectively.

We calculate the electron temperature by assuming that the electrons are heated by Coulomb collisions with protons and helium (Spitzer 1965). We adopt this simple prescription, which gives a lower limit to the equilibration time, knowing that the heating of electrons may, in fact, be far more complicated. For instance, there is reason to believe that collisionless wave-particle interactions with the magnetic turbulence will be important (e.g., Laming 2001), and recent work interpreting hydrogen line widths suggests that the electron-to-proton temperature ratio behind some SNR blast waves depends mainly on the shock speed, a result implying a heating process substantially different from Coulomb collisions (e.g., Ghavamian et al. 2007; Rakowski et al. 2008). However, there remain large uncertainties in connecting the measured line widths to the electron-to-proton temperature ratio (see Heng & Sunyaev 2008), and until particle-in-cell (PIC) simulations are able to model non-relativistic, electron-proton shocks with parameters typical of SNRs, the plasma physics of electron heating will remain uncertain (see Vladimirov, Bykov & Ellison 2008, for a discussion of the limitations of PIC simulations in this regard). In order to model some of the complexity of electron heating, we scale the Coulomb equilibration time with a parameter, f_{eq} , defined in Eq. (3) below.

At the start of the simulation, we assume that the unshocked electrons and ions are in equilibrium at a temperature $T_0 = 10^4$ K. We also assume that unshocked H and He are both 10% singly ionized and all heavier elements are initially neutral. While we note that this is not the precise equilibrium ionization state for 10^4 K, we emphasize that none of our results depend in any significant way on the ionization state of the unshocked material as long as it is not fully neutral. In all of the results shown here we fix the helium number density at 10% of the proton number density, $n_{p,0}$.

At each time-step, we track the ionic state X^i within each spherically symmetric fluid element by solving the

time-dependent ionization equations for each abundant element (H, He, C, N, O, Ne, Mg, Si, S, Ar, Ca, Fe, and Ni). We solve the coupled set of equations with atomic data extracted from Raymond & Smith (1977), as first presented in Gaetz et al. (1988) and updated by Edgar (2008).

In Figure 1 we show an example of the time evolution of the ionization fraction, $f(X^i)$, of high ionization states of oxygen (O^{6+} , O^{7+} and O^{8+}) in a mass shell that is crossed by the forward shock 100 yr after the explosion. For this example, as in all we show in this paper, we have fixed parameters typical of Type Ia supernovae, i.e., the kinetic energy in ejecta from the supernova explosion $E_{SN} = 10^{51}$ erg, the mass of the ejecta $M_{ej} = 1.4M_{\odot}$, the density of the ejecta follows an exponential density profile as is generally assumed for Type Ia supernovae (Dwarkadas 2000), and we assume the supernova explodes in a circumstellar medium (CSM) which is uniform with proton number density $n_{p,0}$ and magnetic field strength B_0 .³ In all of the models shown here, we take $B_0 = 15 \mu\text{G}$.⁴ The figure shows that the density and proton temperature in the shell are dropping with time as the electron temperature increases due to Coulomb collisions. After 1000 yr, the material is close to ionization equilibrium for these ions.

Figure 1 also compares results for test-particle (TP) and efficient DSA. In all of the examples in this paper, we define TP acceleration as being 1% efficient, i.e., 1% of the ram kinetic energy of the forward shock is placed into superthermal particles. For all of our efficient acceleration cases, we assume 75% of the shock ram kinetic energy is placed into superthermal particles, i.e., $\epsilon_{DSA} = 75\%$. Figure 1 shows that efficient DSA produces a higher postshock density and lower postshock temperature, as expected. What is also clear is that the high ionization states of oxygen become populated sooner in the $\epsilon_{DSA} = 75\%$ case. This implies that, instead of suppressing thermal X-ray emission as has been suggested (e.g., Drury et al. 2008; Morlino, Amato & Blasi 2008), efficient DSA can possibly enhance it.

We make the following approximations in the NEI calculation, noting that these are in addition to approximations made in the underlying CR-hydro model (as described in Ellison et al. 2007, and references therein):

- We assume that only electrons from the thermal population contribute to the non-equilibrium ionization. In nonlinear DSA, the energetic population emerges smoothly from the thermal population (a nice example from a relativistic PIC simulation is given in Spitkovsky 2008) and superthermal particles may contribute to ionization (see Porquet et al. 2001, for a test-particle calculation involving a Maxwell-Boltzmann distribution with nonthermal tail). As we discussed above, superthermal particles are expected to contribute to

the ionization at some level. However, the significance of this nonthermal ionization, in shocks undergoing efficient particle acceleration, has not yet been determined and remains an area of active work. For the purposes of this paper, we assume any nonthermal contribution is small.

- We only model the interaction region between the forward shock and the contact discontinuity where we assume cosmic elemental abundances. One reason for emphasizing the forward shock is that it is not certain that significant CR production occurs at the reverse shock in SNRs (e.g., Ellison, Decourchelle & Ballet 2005).
- We only consider young SNRs and do not include the effects of radiative cooling. In the high-density limit, radiative losses could be significant and the cooling time-scale could be comparable to other dynamical time-scales. We will investigate this effect in a subsequent paper.

3. RESULTS

In the following examples we investigate the effect the acceleration efficiency, ϵ_{DSA} , and the CSM proton density, $n_{p,0}$, has on the non-equilibrium ionization state of some selected elements.

3.1. Ionization vs. Position

In Figure 2, we plot the ionization fractions of O^{6+} and O^{7+} and Si^{12+} and Si^{13+} in the top two panels as a function of position behind the forward shock (FS). In all panels, test-particle results ($\epsilon_{DSA} = 1\%$) are shown with dashed curves and efficient DSA results ($\epsilon_{DSA} = 75\%$) are shown with solid curves. The electron density and electron and ion temperatures are shown in the bottom two panels.⁵

As the top two panels clearly show, higher ionization fractions are attained closer to the shock front in the efficient DSA cases, as compared to the TP cases. For instance, in the efficient case, the fraction of O^{7+} peaks at a distance $R/R_{FS} \simeq 0.98$ behind the shock, while in the TP case, this fraction peaks at $R/R_{FS} \simeq 0.97$. We attribute the increased ionization fractions closer to the shock as a direct result of higher postshock densities in the efficient DSA case. Note that the curves extend from the forward shock back to the contact discontinuity, indicating that the region between the forward shock and contact discontinuity is considerably narrower in the efficient acceleration case. This effect produces important morphological consequences (e.g., Decourchelle, Ellison & Ballet 2000; Warren et al. 2005; Cassam-Chenaï et al. 2008).

In Figure 3, we show the same quantities as in Figure 2, except that $n_{p,0} = 0.1 \text{ cm}^{-3}$. The lower CSM density results in lower shocked densities and in less rapid collisional ionization behind the FS. For the ions we show, higher ionization states (i.e., O^{7+} and Si^{12+}) are considerably less populated downstream from the FS when $n_{p,0}$ is small. The differences resulting from DSA are less prominent but still evident; e.g., with $n_{p,0} = 0.1 \text{ cm}^{-3}$, O^{6+} peaks behind the shock at $R/R_{FS} \simeq 0.98$ for the efficient case, and at $\simeq 0.95$ in the test particle case.

⁵ In all results shown, we assume that shocked protons and other ions have the same temperature.

³ We refer the reader to Ellison et al. (2007) for a full discussion of the additional parameters required for the CR-hydro model.

⁴ This value for B_0 is somewhat higher than the typically assumed $3 \mu\text{G}$ and reflects the possibility that magnetic field amplification (MFA) may be taking place. We emphasize, however, that we do not include MFA in the DSA calculation performed here. A large upstream magnetic field, B_0 , will reduce the effects of efficient DSA, as described in Berezhko & Ellison (1999).

To emphasize the importance of the different spatial structures of ionization with ϵ_{DSA} and $n_{p,0}$, we show, in Figure 4, a closeup view of the shock fronts in Figures 2 and 3. Here, we have plotted the ionization fractions as functions of angular distance behind the shock, assuming a distance of 1 kpc. In the high density case ($n_{p,0} = 1 \text{ cm}^{-3}$; top panel), the fraction of O^{6+} peaks right behind the shock at $\sim 2''$ downstream, while it peaks $\sim 5''$ behind the shock in the test particle case. In the lower density case ($n_{p,0} = 0.1 \text{ cm}^{-3}$; lower panel), O^{6+} peaks $\sim 30''$ behind the shock in the efficient case, but peaks well beyond $50''$ behind the shock in the test particle case. Similar results are found for silicon. While these models are not scaled to match any particular Galactic SNR, we believe the angular separations shown here would be easily resolvable in current and future space-based X-ray observatories even when line-of-sight effects are taken into account. Thus, measuring the relative fraction of H-like, He-like, and even Li-like charge states would provide a useful diagnostic in studies of Galactic SNRs undergoing efficient shock acceleration.

Another interesting feature seen in Figures 2 and 3, is that the electron temperature is almost independent of ϵ_{DSA} and only varies by a factor of ~ 2 between the $n_{p,0} = 1 \text{ cm}^{-3}$ and $n_{p,0} = 0.1 \text{ cm}^{-3}$ cases. This is in contrast to the ion temperatures, where generally lower ion temperatures occur in the higher density models, due to the lower shock Mach number, and where the large ϵ_{DSA} cases have considerably lower ion temperatures than the test-particle cases. The fact that lower postshock temperatures occur in efficient DSA is well known (e.g., Ellison 2000). The electron temperature is influenced by this and by the higher densities that occur with efficient DSA. The higher postshock densities imply more collisions between electrons and ions, and thus more rapid temperature equilibration. The higher electron temperature combined with the higher postshock density leads to more rapid ionization, and thus higher charge states closer to the forward shock.

3.2. Ionization vs Equilibration Timescale

As is clear from Figures 1, 2, and 3, the ionization fraction for high charge state ions can increase with acceleration efficiency. Since the electron temperature is almost independent of $n_{p,0}$ in these cases, we attribute this effect mainly to the higher postshock densities. However, we have assumed a particular model for temperature equilibration between protons and electrons, namely that electrons start off cold and equilibration with the hot protons occurs only through Coulomb collisions where the equilibration timescale is given by (Spitzer 1965, Eq. 5-31):

$$t_{\text{eq}} = \frac{3m_p m_e k_B^{3/2}}{8(2\pi)^{1/2} n_p Z^2 e^4 \ln \Lambda} \left(\frac{T_p}{m_p} + \frac{T_e}{m_e} \right)^{3/2}. \quad (2)$$

Here, m_p is the proton mass and T_p is the shocked proton temperature and definitions of the other terms are given in Spitzer (1965). It's important to note that Eq. (2) places strict limits on how low the electron to proton temperature ratio can be behind the shock (see Hughes, Rakowski & Decourchelle 2000); if other equilibration mechanisms are important, such as plasma wave interactions, equilibration will occur more rapidly. To investigate the effects of more rapid temperature equilibration, we define a parameter, $0 \leq f_{\text{eq}} \leq 1$, and use the

equilibration time t'_{eq} in our calculations where,

$$t'_{\text{eq}} = f_{\text{eq}} t_{\text{eq}}. \quad (3)$$

In the results shown in Figures 1, 2, 3, and 4, we have assumed $f_{\text{eq}} = 1$.

In Figure 5, we compare the ionization fraction of O^{7+} for $\epsilon_{\text{DSA}} = 1\%$ and $\epsilon_{\text{DSA}} = 75\%$ calculated with $f_{\text{eq}} = 1$ (black curves in all panels) and $f_{\text{eq}} = 0.1$ (red curves in all panels). For both values of ϵ_{DSA} , $f(\text{O}^{7+})$ is larger immediately behind the shock for rapid equilibration ($f_{\text{eq}} = 0.1$) but drops below the $f_{\text{eq}} = 1$ value further downstream as O^{8+} becomes populated. The temperature plots in the bottom two panels show that the electrons and protons have come into equilibrium for a range of radii (i.e., $0.86 \lesssim R/R_{\text{FS}} \lesssim 0.98$) when $\epsilon_{\text{DSA}} = 75\%$ and $f_{\text{eq}} = 0.1$, but remain far from equilibrium for $f_{\text{eq}} = 1$ regardless of ϵ_{DSA} . The equilibration rate changes the ionization structure for this particular ion, producing changes comparable in scale to those produced by efficient DSA.

To quantify these effects further, we look at a point midway between the contact discontinuity and FS, i.e., at $R/R_{\text{FS}} \simeq 0.89$ for $\epsilon_{\text{DSA}} = 75\%$ and at $R/R_{\text{FS}} \simeq 0.83$ for $\epsilon_{\text{DSA}} = 1\%$ in Figure 5. At these locations, the electron to proton temperature ratios are: $(T_e/T_p)_{\text{TP}} \simeq 0.11$ and $(T_e/T_p)_{\text{NL}} \simeq 0.36$, for $f_{\text{eq}} = 1$, and $(T_e/T_p)_{\text{TP}} \simeq 0.3$ and $(T_e/T_p)_{\text{NL}} = 1$ for $f_{\text{eq}} = 0.1$, i.e., the ratios are about 3 times larger with rapid equilibration. At these midpoint locations, the ionization fractions of O^{7+} range from $f(\text{O}^{7+}) \simeq 0.05$ for $f_{\text{eq}} = 1$ and $\epsilon_{\text{DSA}} = 75\%$, to $f(\text{O}^{7+}) \simeq 0.23$ for $f_{\text{eq}} = 0.1$ and $\epsilon_{\text{DSA}} = 1\%$, i.e., about a factor of five span.

The electron temperature ratio for $f_{\text{eq}} = 1$ is $(T_{e,\text{NL}}/T_{e,\text{TP}})_{f_{\text{eq}}=1} = 1.8 \times 10^7 \text{ K} / 2.5 \times 10^7 \text{ K} \simeq 0.7$ and the ratio for $f_{\text{eq}} = 0.1$ is $(T_{e,\text{NL}}/T_{e,\text{TP}})_{f_{\text{eq}}=0.1} = 3 \times 10^7 \text{ K} / 6 \times 10^7 \text{ K} \simeq 0.5$. For the particular parameters used in this example, the electron temperature stays within a factor of ~ 2 for a wide spread in ϵ_{DSA} and equilibration time, while $f(\text{O}^{7+})$ varies by a factor of ~ 5 .

3.3. Emission Measure vs. Acceleration Efficiency

As seen in Figures 2 or 3, the plasma density is greatest immediately behind the shock where the electron temperature is lowest. Since the rate for electron temperature equilibration depends on the proton temperature and density and both the temperature and density depend on ϵ_{DSA} , the NEI calculation will depend in a complicated fashion on the forward shock dynamics and the evolution of the interaction region between the CD and FS. Of course, the important property is the emission the plasma produces and this can be characterized by the emission measure (EM) and the differential emission measure (DEM).

In Figure 6 we plot the emission measure for individual ions, $\text{EM} = N_X f(X^i, R) n_e n_p dV$, and in Figure 7 we plot ionic differential emission measures, $\text{DEM} = \sum N_X f(X^i, R) n_e n_p dV / d(\log T_e)$, where N_X is the abundance of element X relative to hydrogen, $f(X^i, R)$ is the ionization fraction for the ion X^i at a distance R behind the shock, and dV is the volume of the shell where EM or DEM is determined. The EM plotted in Figure 6 is a line-of-sight projection normalized to 1 cm^2 surface area,

and the DEM is obtained by summing over the region between the CD and FS.

Figure 6 clearly shows that the emission for these ions peaks much closer to the FS and is considerably stronger with efficient DSA than in the TP case. Figure 7 shows that the peak emission for these two ions shifts down in temperature by about a factor of ~ 2 (~ 1 keV) when efficient DSA occurs. These two effects are quite significant for individual ions and should be observable. Nevertheless, the emission from a full set of ions needs to be calculated and the results folded through a detectors' response before the signature of efficient DSA can be quantitatively determined.

4. DISCUSSION AND CONCLUSIONS

We have presented a calculation of non-equilibrium ionization in a hydrodynamic simulation of SNRs undergoing efficient DSA. While we have only explored a limited range of parameters in this paper, it's clear that the production of CRs by the outer blast wave modifies the SNR evolution and structure enough to produce significant changes in the ionization of the shocked material between the forward shock and contact discontinuity. In particular, *higher ionization states are reached at lower electron temperatures* (compared to the test particle case) because of the increase in post shock density due to the increased shock compression. The calculation of thermal X-ray line emission requires the additional step of coupling the resultant ionization state vectors to a plasma emissivity code, work which is in progress. Nevertheless, our results clearly show that taking DSA into account and dynamically calculating the NEI produces changes in the ionization fractions of important elements that should translate into noticeable changes in the interpretation of X-ray line emission observed from young SNRs.

Our main results are the following:

- Compared to the test-particle case, the increase in ionization that accompanied DSA in our examples suggests that efficient DSA will result in an increase in the overall thermal X-ray emission (see Figure 6). We note that an increase in thermal emission with increasing acceleration efficiency is evident in our earlier results which explored a slightly different parameter space (i.e., Figures 7 and 8, Ellison et al. 2007). The actual increase may depend importantly on other model parameters, such as the CSM density, and it is important to explore a more expanded parameter space to determine how broadly valid our results are. This work is in progress. However, regardless of whether or not efficient DSA increases the integrated thermal emission over the test-particle case, some thermal emission is expected because ionization is not suppressed when efficient DSA occurs. As Figure 1 shows, electrons reach X-ray emitting temperatures well before they come into equilibration with protons and nearly as rapidly with or without efficient DSA. This occurs even if only Coulomb equilibration is assumed. This is in contrast to recent claims (e.g., Morlino, Amato & Blasi 2008; Drury et al. 2008) that very weak thermal X-ray emission might result from efficient shock acceleration.

- Compared to the test-particle case, ionization occurs more rapidly and, therefore, closer to the FS, with efficient acceleration (see Figures 4 and 6). The differences in spatial structure should be large enough to observe and may be used as a discriminant for the level of CR-modification, if a particular ion state is coupled to other known properties, such as the dynamics and ambient conditions.
- Efficient DSA leads to more efficient Coulomb heating of electrons and faster equilibration with ions, relative to the test particle case. This results because the shocked plasma temperature is lower and the shocked density is higher when efficient DSA occurs. We showed, with a simple parameterization of the thermal equilibration time, that the signature of efficient DSA on the ionization state remains apparent for equilibration more rapid than occurs with just Coulomb collisions.
- Using the differential emission measure, we showed that the maximum emission from a particular ion state occurs at a significantly lower electron temperature with efficient DSA. For the ions shown in Figure 7, the difference in T_e for peak emission is on the order of 1 keV while the maximum DEM remains almost constant. A difference this large will have an important impact on the interpretation of thermal X-ray emission in young SNRs.

Currently, we do not treat radiative or slow shocks, but these regimes are easily explored. For instance in a radiative shock, the cooling time might be comparable to the energy loss time in a cosmic ray modified shock. Increases in the density will enhance the cooling to the point where radiative losses might rival losses from efficient DSA (Wagner et al. 2006). We intend to explore this regime in a forthcoming paper.

While we only considered shocked CSM here, we will consider shocked ejecta in future work. In the ejecta, the electron density can be higher and the temperature may be lower but, more importantly, the abundance structure is far more complicated than for CSM and calculations of X-ray emission are intrinsically more difficult. Furthermore, simple arguments based on the expansion of the ejecta material suggest that the magnetic field may be too low to support DSA by the reverse shock. Nevertheless, there has been speculation that particles are accelerated there (e.g., Gotthelf et al. 2001; Uchiyama & Aharonian 2008; Helder & Vink 2008) and if DSA is efficient at the reverse shock, it will likely alter the ionization balance of the shocked ejecta as much as shown here for the shocked CSM.

Finally, while we have limited our examples here to SNRs expanding into a uniform medium typical of Type Ia supernovae, we emphasize that a wider parameter space should be explored, in terms of both the structure of the ambient medium (i.e. pre-SN winds) and the parameters which determine the cosmic ray acceleration efficiency. These cases will be addressed in a follow-up paper.

We would like to thank Dick Edgar, John Raymond, and Cara Rakowski for several useful discussions on how

to thoughtfully display and interpret ionization fractions. This work was partially supported through a Smithsonian Endowment Grant. D. J. P. and P. O. S. ac-

knowledge support from NASA contract NAS8-39073 and D.C.E acknowledges support from NASA grants NNNH04Zss001N-LTSA and 06-ATP06-21.

REFERENCES

- Aharonian, F.A. et al. 2007 (HESS collaboration), *A&A*, 464, 235
 Amato, E. & Blasi, P. 2005, *MNRAS*, 364, L76
 Bamba, A., et al. 2008, *Advances in Space Research*, 41, 411
 Berezhki, E. G. & Ellison, D. C. *ApJ*, 526, 385
 Blasi, P., Gabici, S., & Vannoni, G. 2005, *MNRAS*, 361, 907
 Cassam-Chenaï, G., Hughes, J. P., Ballet, J., & Decourchelle, A. 2007, *ApJ*, 665, 315
 Cassam-Chenaï, G., Hughes, J. P., Reynoso, E. M., Badenes, C. & Moffett, D. 2008, *ApJ*, 680, 1180
 Decourchelle, A., Ellison, D.C., & Ballet, J. 2000, *ApJ*, 543, L57
 Drury, L. O., Aharonian, F.A., Malyshev, D. & Gabici, S. 2008, preprint 0811.3566
 Dwarkadas, V. V. 2000, *ApJ*, 541, 418
 Edgar, R. J. 2008, private communication
 Ellison, D.C. 2000, *AIP Conf. Proc.* 528, *Acceleration and Transport of Energetic Particles Observed in the Heliosphere*, ed. R. A. Mewaldt, J. R. Jokipii, M. A. Lee, E. Möbius, & T. H. Zurbuchen (New York: AIP), p. 386
 Ellison, D. C. & Cassam-Chenaï, G. 2005, *ApJ*, 632, 920
 Ellison, D. C. and Decourchelle, A. and Ballet, J. 2005, *A&A*, 429, 569
 Ellison, D. C., Patnaude, D. J., Slane, P., Blasi, P., & Gabici, S. 2007, *ApJ*, 661, 879
 Ellison, D. C., Slane, P. & Gaensler, B. M. 2001, *ApJ*, 563, 191
 Gaetz, T. J., Edgar, R. J., & Chevalier, R. A. 1988, *ApJ*, 329, 927
 Ghavamian, P., Laming, J. M., & Rakowski, C. E. 2007, *ApJ*, 654, L69
 Gotthelf, E. V., Koralesky, B., Rudnick, L., Jones, T. W., Hwang, U. & Petre, R. 2001, *ApJ*, 552, L39
 Helder, E. A., & Vink, J. 2008, *ApJ*, submitted
 Heng, K. & Sunyaev, R. A. 2008, *A&A*, 481, 117.
 Hughes, J. P., Rakowski, C. E. & Decourchelle, A. 2000, *ApJ*, 543, L61
 Hwang, U., Decourchelle, A., Holt, S. S., & Petre, R. 2002, *ApJ*, 581, 1101
 Jones, F. C. & Ellison, D. C. 1991, *Space Sci. Rev.*, 58, 259
 Katz, B. & Waxman, E. 2008, *JCAP*, 1, 18
 Laming, J. M. 2001, *ApJ*, 563, 828
 Morlino, G., Amato, E. & Blasi, P. 2008, *MNRAS*, preprint
 Porquet, D., Arnaud, M., & Decourchelle, A. 2001, *A&A*, 373, 1110
 Rakowski, C. E., Laming, J. M., & Ghavamian, P. 2008, *ArXiv e-prints*, 805, arXiv:0805.3084
 Raymond, J. C., & Smith, B. W. 1977, *ApJS*, 35, 419
 Reynolds, S. P., Borkowski, K. J., Hwang, U., Hughes, J. P., Badenes, C., Laming, J. M., & Blondin, J. M. 2007, *ApJ*, 668, L135
 Slane, P., Gaensler, B. M., Dame, T. M., Hughes, J. P., Plucinsky, P. P., & Green, A. 1999, *ApJ*, 525, 357
 Spitkovsky, A. 2008, in press, *ArXiv e-prints*: 0802.3216
 Spitzer, L. 1965, *Interscience Tracts on Physics and Astronomy*, New York: Interscience Publication, 1965, 2nd rev. ed.
 Uchiyama, Y., & Aharonian, F. A. 2008, *ApJ*, 677, L105
 van Adelsberg, M., Heng, K., McCray, R., & Raymond, J. C. 2008, *ArXiv e-prints*, 803, arXiv:0803.2521
 Vink, J., Laming, J. M., Gu, M. F., Rasmussen, A., & Kaastra, J. S. 2003, *ApJ*, 587, L31
 Vink, J., Bleeker, J., van der Heyden, K., Bykov, A., Bamba, A., & Yamazaki, R. 2006, *ApJ*, 648, L33
 Vladimirov, A., Bykov, A., & Ellison, D. C., 2008, *ApJ*, in press.
 Wagner, A. Y., Falle, S. A. E. G., Hartquist, T. W., & Pittard, J. M. 2006, *A&A*, 452, 763
 Warren, J.S. et al. 2005, *ApJ*, 634, 376
 Yamaguchi, H., Koyama, K., Nakajima, H., Bamba, A., Yamazaki, R., Vink, J., & Kawachi, A. 2008, *PASJ*, 60, 123

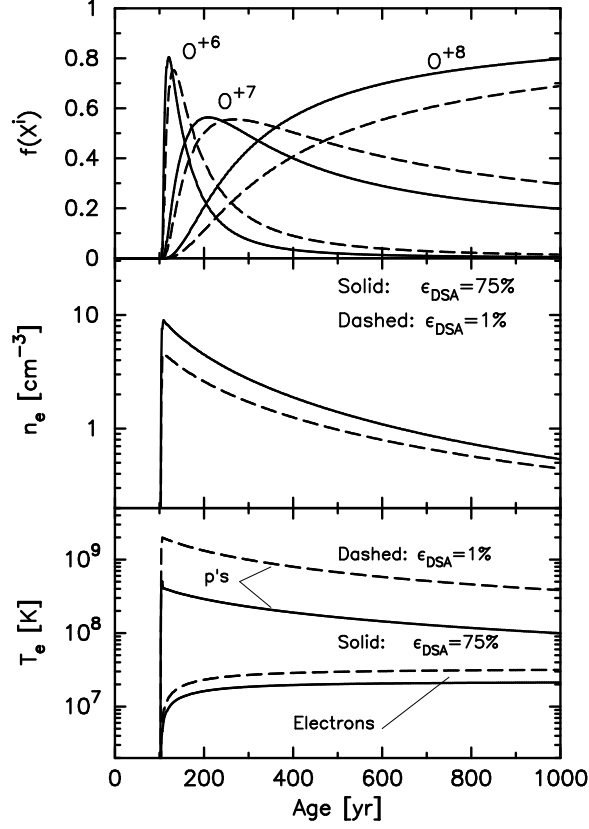


FIG. 1.— Time evolution of a spherically symmetric Lagrangian mass shell which is crossed by the forward shock at 100 yr. The top panel shows the evolution of high ionization states of oxygen, the middle panel shows the electron number density, and the bottom panel shows the electron and proton temperatures, assuming Coulomb equilibration. In all panels, the solid curves correspond to a model with 75% DSA efficiency, while the dashed curves are for a TP model with $\epsilon_{\text{DSA}} = 1\%$. The CSM proton number density for this example is $n_{p,0} = 1 \text{ cm}^{-3}$. Here, and in all other examples, the unshocked CSM temperature is $T_0 = 10^4 \text{ K}$, and the unshocked magnetic field is $B_0 = 15 \mu\text{G}$.

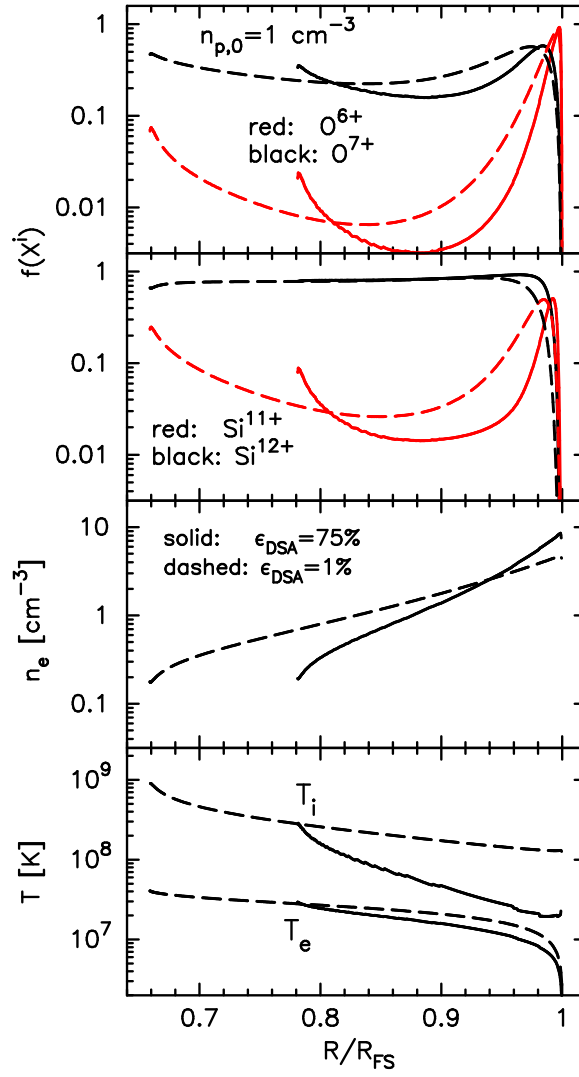


FIG. 2.— Spatial profiles of H- and He-like oxygen and silicon, electron density, and temperature as a function of distance behind the forward shock. In the bottom panel, the curves labeled T_i are ion (or proton) temperatures and those T_e are electron temperatures. Here, and in figures 3-5 that follow, we show values from spherically symmetric shells as a function of R or ΔR , not line-of-sight projections. In all panels, solid curves correspond to models with 75% efficiency, while the dashed lines correspond to TP models. These models are for a CSM proton density of $n_{p,0} = 1 \text{ cm}^{-3}$ and are calculated at $t_{\text{SNR}} = 1000 \text{ yr}$. In the model with 75% efficiency, the forward shock velocity is $\approx 1800 \text{ km s}^{-1}$, while in the test particle model, it is $\approx 2200 \text{ km s}^{-1}$ at $t_{\text{SNR}} = 1000 \text{ yr}$.

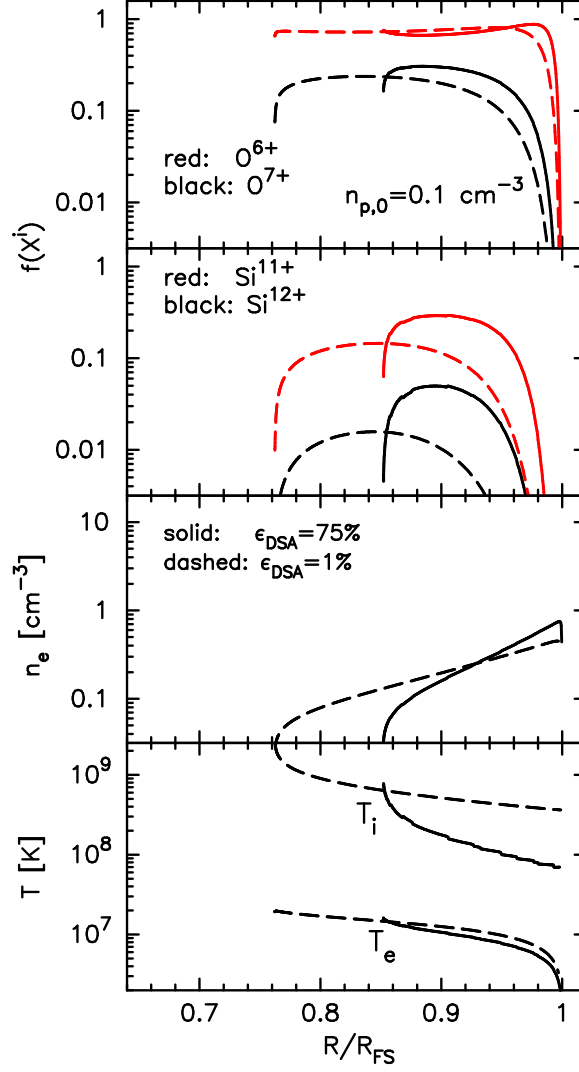


FIG. 3.— Spatial profiles of oxygen and silicon ions, electron density, and temperature as a function of distance behind the forward shock. In all panels, solid curves correspond to models with 75% efficiency, while the dashed lines correspond to TP models. These models are for a CSM proton density $n_{p,0} = 0.1 \text{ cm}^{-3}$ and are calculated at $t_{\text{SNR}} = 1000 \text{ yr}$. In the model with 75% efficiency, the forward shock velocity is $\approx 3200 \text{ km s}^{-1}$, while in the test particle model, it is $\approx 3600 \text{ km s}^{-1}$ at $t_{\text{SNR}} = 1000 \text{ yr}$.

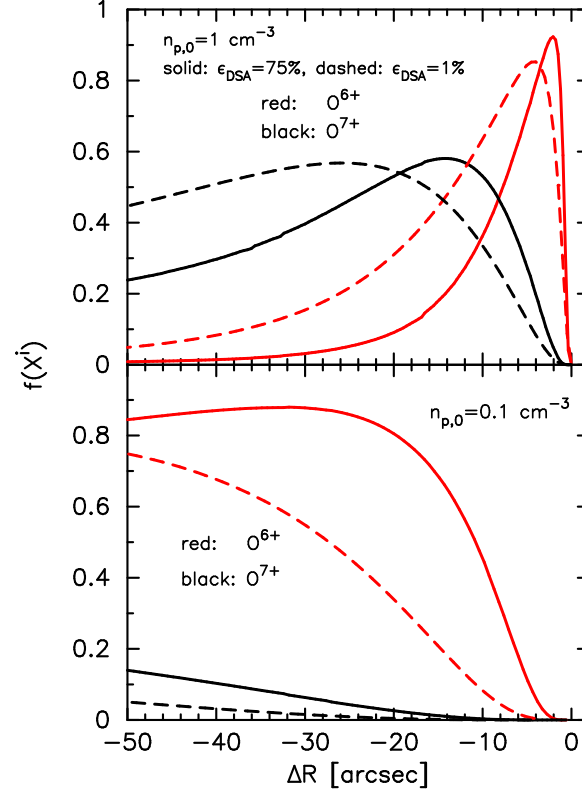


FIG. 4.— *Top:* Ionization fraction as a function of distance behind the forward shock for O^{6+} and O^{7+} with $n_{p,0} = 1.0 \text{ cm}^{-3}$. *Bottom:* Ionization fractions of O^{6+} and O^{7+} with $n_{p,0} = 0.1 \text{ cm}^{-3}$. In both panels, the solid curves are for $\epsilon_{\text{DSA}} = 75\%$ and the dashed curves are for $\epsilon_{\text{DSA}} = 1\%$. The angular scale is determined assuming the SNR is at a distance of 1 kpc and the results are calculated at $t_{\text{SNR}} = 1000 \text{ yr}$.

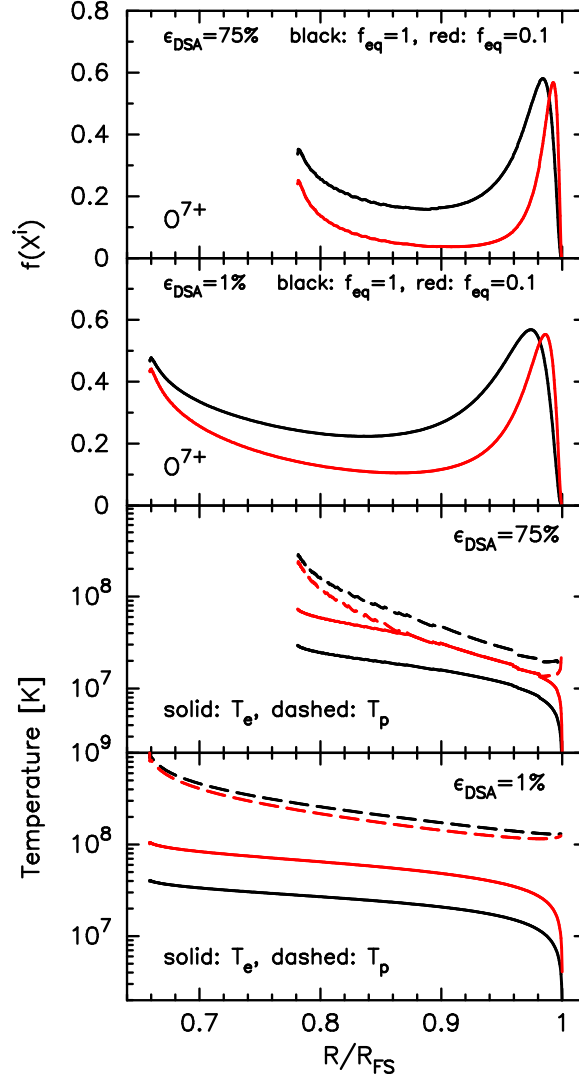


FIG. 5.— Ionization fraction and temperature calculated between the contact discontinuity and FS. All calculations are at $t_{\text{SNR}} = 1000$ yr and assume $n_{p,0} = 1 \text{ cm}^{-3}$. In all panels, black curves assume $f_{\text{eq}} = 1$ and red curves assume $f_{\text{eq}} = 0.1$. In the bottom two panels, the solid curves are the shocked electron temperature, T_e , and the dashed curves are the shocked proton temperature, T_p . As in Figures 2 and 3, the left end of each curve is at the position of the CD.

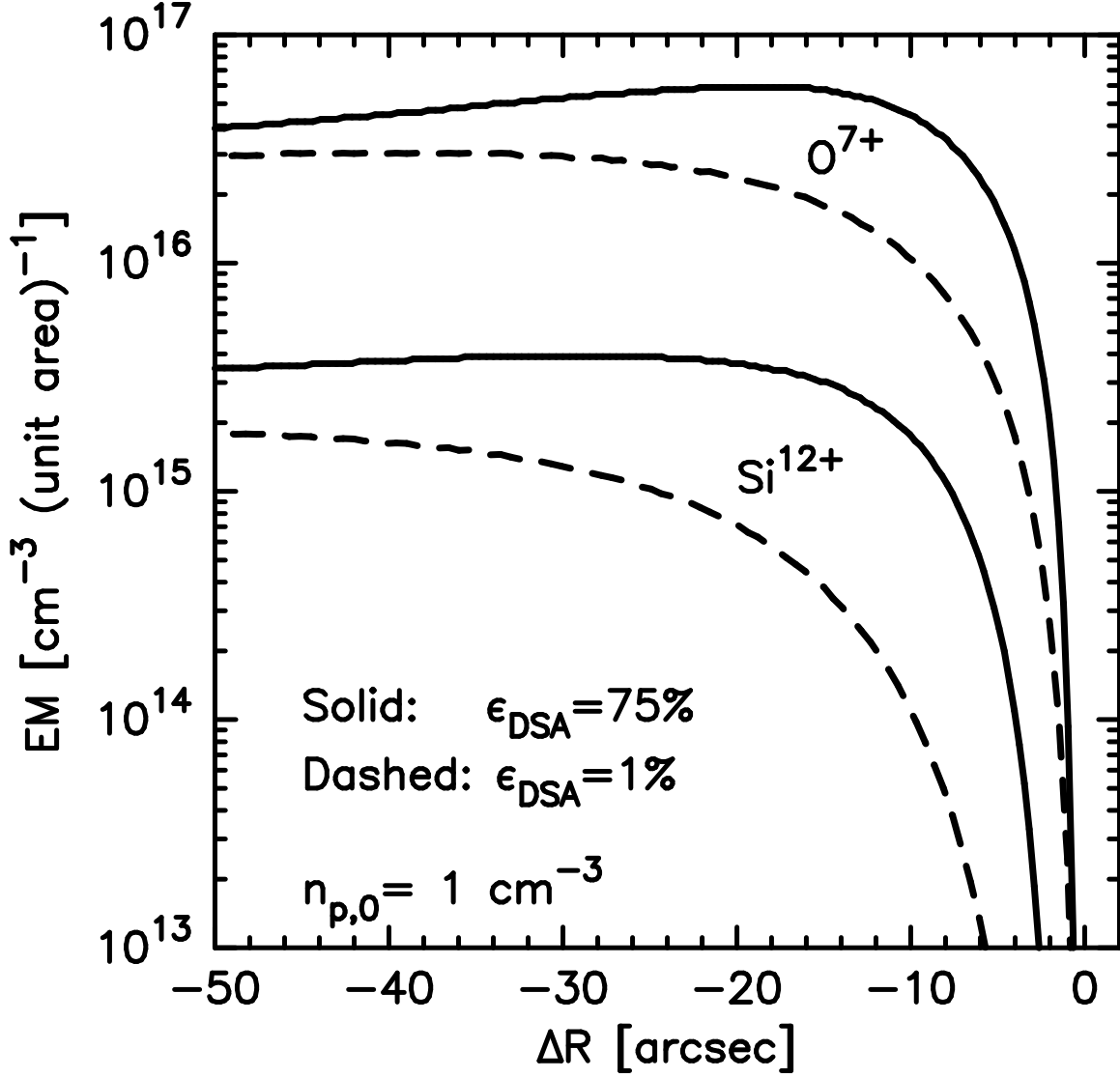


FIG. 6.— Line-of-sight projection of the emission measure (EM) for O^{7+} and Si^{12+} as labeled. The solid curves are for $\epsilon_{\text{DSA}} = 75\%$ and the dashed curves are for $\epsilon_{\text{DSA}} = 1\%$. The angular distance, ΔR , from the FS is determined assuming the SNR is at 1 kpc and the results are calculated at $t_{\text{SNR}} = 1000 \text{ yr}$ with $n_{p,0} = 1 \text{ cm}^{-3}$ and $t_{\text{eq}} = 1$.

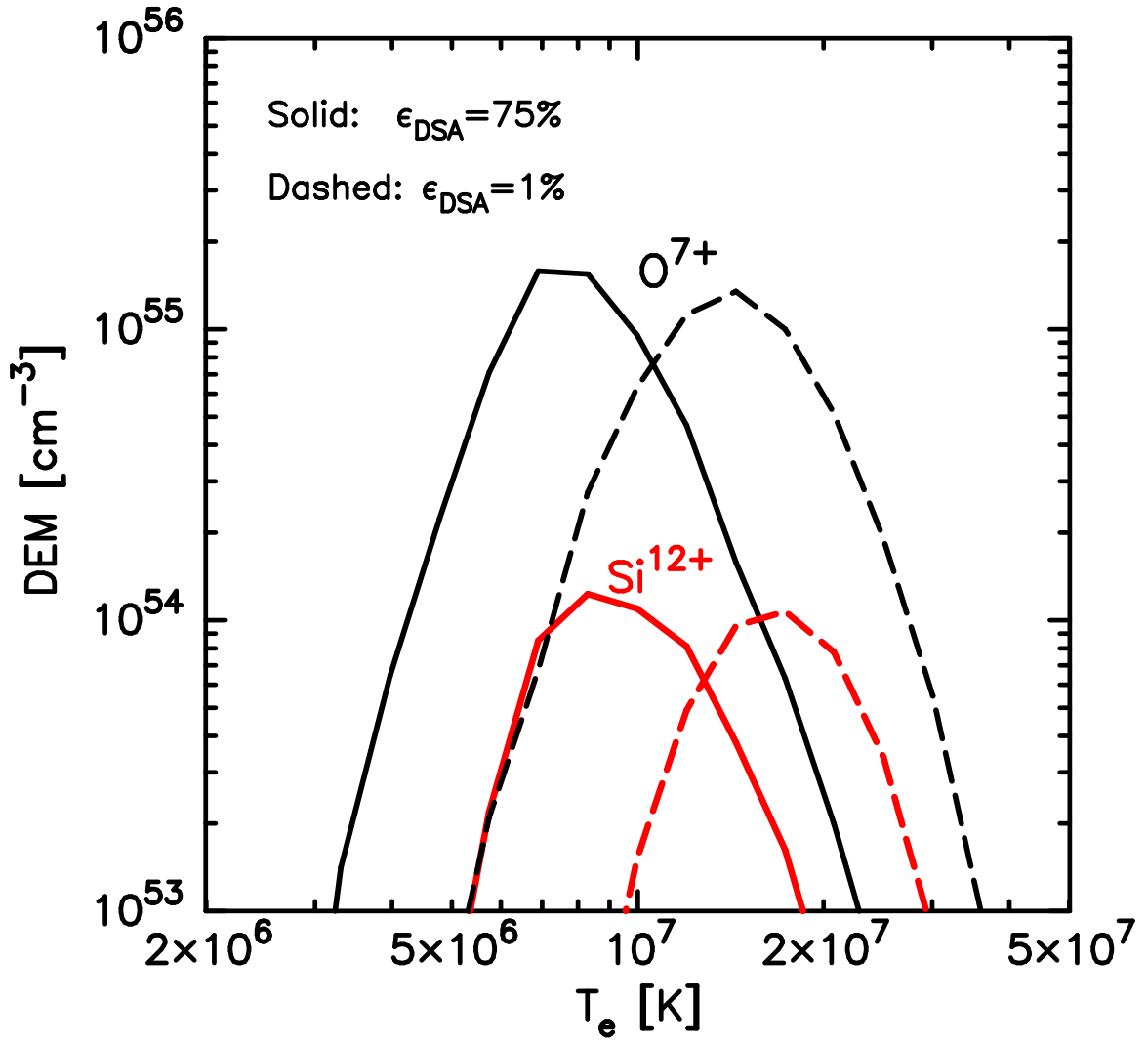


FIG. 7.— Differential emission measure (DEM) vs. electron temperature for O^{7+} and Si^{12+} as labeled. The solid curves are for $\epsilon_{\text{DSA}} = 75\%$ and the dashed curves are for $\epsilon_{\text{DSA}} = 1\%$. The results are calculated at $t_{\text{SNR}} = 1000 \text{ yr}$ with $n_{p,0} = 1 \text{ cm}^{-3}$ and $t_{\text{eq}} = 1$.